# 1 Heterometallic seed-mediated growth of monodisperse

## 2 colloidal copper nanorods with widely tunable

## **3 plasmonic resonances**

- 5 Soojin Jeong, Yang Liu, Yaxu Zhong, Xun Zhan, Yuda Li, Yi Wang, Phoebe M. Cha, Jun Chen,
- 6 Xingchen Ye\*

7

4

- 8 Department of Chemistry, Indiana University, 800 East Kirkwood Avenue, Bloomington, Indiana 47405,
- 9 USA.
- \* Correspondence should be addressed to X.Y. (xingye@indiana.edu).

- 12 KEYWORDS. Cu nanorods, seed-mediated growth, localized surface plasmon resonance,
- coherent nano-area electron diffraction

## 1 ABSTRACT

We report a heterometallic seed-mediated synthesis method for monodisperse penta-twinned Cu nanorods using Au nanocrystals as seeds. Elemental analyses indicate that resultant nanorods consist predominantly of copper with a gold content typically below 3 at. %. The nanorod aspect ratio can be readily adjusted from 2.8 to 13.1 by varying the molar ratio between Au seeds and Cu precursor, resulting in narrow longitudinal plasmon resonances tunable from 762 to 2201 nm. Studies of reaction intermediates reveal that symmetry-breaking is promoted by rapid nanoscale diffusion in Au-Cu alloys and the formation of a gold-rich surface. The growth pathway features co-evolving shape and composition whereby nanocrystals become progressively enriched with Cu concomitant with nanorod growth. The availability of uniform colloidal Cu nanorods with widely tunable aspect ratios opens new avenues toward the synthesis of derivative one-dimensional metal nanostructures, and applications in surface-enhanced spectroscopy, bioimaging, electrocatalysis, among others.

## 1 INTRODUCTION

2

3

4

5

6

7

8

9

10

11

12

13

14

15

16

17

18

19

20

21

22

23

24

25

26

27

28

29

30

Over past few decades, metal nanorods (NRs) as an important class of one-dimensional nanomaterials have attracted great interest owing to their superior plasmonic, catalytic and electrical properties.<sup>1</sup> Colloidal gold<sup>2, 3</sup> and silver<sup>4-6</sup> NRs exhibiting aspect-ratio-dependent longitudinal surface plasmon resonance (LSPR) have enabled myriad applications in surface-enhanced spectroscopy,<sup>7,8</sup> plasmon-enhanced photocatalysis,<sup>9</sup> near-infrared (NIR) bioimaging and therapeutics,<sup>10</sup> etc. Cu is an earth-abundant and inexpensive metal. Nanostructured copper is well suited for transparent conductors<sup>11, 12</sup> and catalytic applications ranging from electroreduction of CO<sub>2</sub> and CO to liquid fuels,<sup>13</sup> methanol synthesis<sup>14</sup> to Ullmann coupling reaction.<sup>15</sup> Although SPR on copper can be strongly damped in the visible range due to its low onset of interband transitions (2.1 eV), a high-quality-factor SPR rivaling gold and silver becomes realistic with copper provided that the resonance frequency can be shifted into the infrared spectral region.<sup>16</sup>

Despite the tremendous progress made toward the synthesis of coinage metal nanocrystals (NCs), shape-controlled Cu NCs remains far less developed compared to systems like gold and silver. 17-19 One major obstacle lies in the insufficient understanding of dynamic speciation of copper under reaction conditions and kinetic pathways by which Cu precursors are converted into metallic Cu. 19, 20 Another complicating factor is that nanoscale copper has a strong tendency to oxidize especially in aqueous solutions. 17, 21 Among one-dimensional Cu nanomaterials, there has been far fewer examples of NRs than nanowires, which highlights the difficulty in avoiding elongated Cu nanostructures to rapidly develop into nanowires. In one early study, Cu NRs were synthesized via hydrazine reduction of copper(II) bis(2-ethylhexyl) sulfosuccinate (Cu(AOT)<sub>2</sub>) in an isooctane-water mixture.<sup>22</sup> A bicontinuous network of cylindrical micelles was proposed to template the growth and the yield of NR was ca. 40% with remaining products largely spherical NCs. Later, Zhong and coworkers reported a non-aqueous synthesis of Cu NRs using 1,2hexadecanediol as the reducing agent. However, a mixture of nanospheres, nanocubes and NRs was obtained with low shape selectivity.<sup>23</sup> Apart from the seedless approach, multiple seedmediated methods have been developed for Cu NRs. Yin et al. reported seeded growth of Cu NRs onto single-crystalline Au seeds. The large lattice mismatch between Cu and Au (11.4%) was proposed to induce twinning and promote lateral growth into tapered NRs.<sup>24</sup> Xia et al. used pentatwinned Pd seeds to direct the growth of Cu NRs exhibiting tunable LSPRs from visible to 1100

- 1 nm.<sup>21</sup> Transmission electron microscopy (TEM) revealed that the Pd seed was retained at one end
- of each Cu NR, suggesting that seeds play a key role in symmetry breaking. More recently, Yin
- 3 and coworkers developed a space-confined seeded growth strategy to prepare Cu NRs with tunable
- 4 LSPR from 935 to 1290 nm. 25 Despite these significant advances, the demand for monodisperse
- 5 Cu NRs with widely tunable aspect ratios (ARs) and dimensions motivates further synthetic
- 6 development and improved mechanistic understanding of growth pathways.
- 7 Here, we report a heterometallic seed-mediated method for Cu NRs with uniform diameters and
- 8 variable lengths using preformed Au NCs as seeds. Elemental analyses indicated that as-formed
- 9 NRs consist predominantly of copper with a gold content typically below 3 at. %. By changing the
- molar ratio between Au seeds and Cu precursor, the AR of NRs can be readily varied from 2.8 to
- 13.1, producing sharp LSPRs tunable from 762 to 2201 nm. We further uncovered the critical roles
- of alloying and diffusion in initiating and sustaining anisotropic growth by analyzing reaction
- intermediates.

15

16

17

18

19

20

21

22

23

24

25

26

27

28 29

30

## RESULTS AND DISCUSSION

Figure 1a illustrates the synthetic scheme of Cu NRs where oleylamine (OLAM) was employed as both the reducing agent and solvent. A Cu(II)-OLAM complex formed as the reaction mixture was heated to 80 °C, producing a transparent blue solution. Reduction of Cu(II) to Cu(I) occurred when the temperature reached 180 °C, as indicated by the color change from blue to light yellow. 12 Growth of Cu NRs was initiated by adding Au NCs into the reaction solution at 180 °C. Figure 1b shows a TEM image of 9.0 nm OLAM-capped Au seeds which provided heterogeneous nucleation sites for incoming Cu atoms. Without Au seeds, no Cu NCs formed even after heating the reaction mixture at 180 °C for two hours. Figure 1c shows a TEM image of as-synthesized NRs with a mean diameter and length of 12.5 and 100 nm, respectively. Scanning TEM energy-dispersive Xray spectroscopy (STEM-EDS) analysis revealed that each NR was composed predominantly of Cu with residual Au (2%) evenly distributed throughout (Figure 1d,e). Scanning electron microscope EDS (SEM-EDS) which surveyed a wide area (~10 μm<sup>2</sup>) containing nearly 10,000 NRs also indicated a trace amount of gold present (Figure 1f). X-ray diffraction (XRD) pattern showed three prominent peaks at 43.1°, 50.2°, and 73.7°, which best matched with the (111), (200), and (220) diffractions of the face-centered cubic (fcc) Au<sub>0.03</sub>Cu<sub>0.97</sub> phase (Figure 1g). Considering the insignificant differences in lattice parameters of Au<sub>0.03</sub>Cu<sub>0.97</sub> (3.63 Å) and Cu (3.62 Å), the NRs

obtained were essentially Cu NRs, which is distinct from previous reports of Cu-containing NRs with much higher contents of secondary metals such as Au and Pd.<sup>26-28</sup> The extra peak at 37.5° is attributed to Cu<sub>2</sub>O, a common oxidation product of copper at ambient conditions (Figure 1g).<sup>15</sup>

Figure 2a shows a representative HRTEM image of a NR (AR=10.6). Two sets of fringes with 4 lattice spacings of 2.25 and 1.44 Å were observed, corresponding to the (111) and (220) planes of 5 fcc Cu, respectively. We further used coherent nano-area electron diffraction (CNED) to probe NR 6 structure (Figure 2c).<sup>29</sup> The CNED pattern cannot be indexed as a single zone-axis pattern of fcc 7 Cu, suggesting that they are not single-crystalline (Figure 2d). Close examination revealed that 8 most spots can be accounted for based on the superposition of <111> and <110> diffractions. This 9 interpretation indicates that these NRs have a cyclic penta-twinned structure with five {111}-type 10 twin boundaries arranged radially along the common [110] longitudinal direction, in agreement 11 with previous results obtained for multi-twinned metal NRs and nanowires. 12, 30, 31 The remaining 12 diffraction spots are attributed to double diffractions from differently oriented crystalline domains 13 and Cu<sub>2</sub>O on NR surface (Figure S1). The five-fold axial symmetry was also confirmed with nano-14 15 beam electron diffraction (NBED, Figure 2e) that used a convergent beam to probe the local structure of materials (Figure 2c). The NR orientation in Figure 2a,c is schematically illustrated in 16 Figure 2b. A pentagonal cross-section showing five face-sharing fcc domains labelled as T1 to T5 17 is highlighted when viewed along the [110] central axis. HRTEM image taken from a different but 18 19 perhaps more commonly observed NR orientation is shown in Figure 2f, where continuous {111} lattice fringes running parallel to the long axis were readily resolved. Notably, Moiré patterns 20 consisting of wide dark stripes appeared along the central region.<sup>30, 31</sup> The CNED and NBED 21 patterns acquired at this orientation can be interpreted as the combination of <112> and <100> 22 diffractions (Figure 2h-j). This NR orientation, as depicted in Figure 2g, is related to the diagram 23 shown in Figure 2b by an 18° rotation around the five-fold axis. Rather than having the electron 24 beam parallel to one of the side facets (Figure 2b), in this configuration, the electron beam runs 25 perpendicular to one side surface of NR (Figure 2g). Consequently, overlap between [100]-26 oriented T1 domain and [112]-oriented T3 and T4 domains is satisfied only in the central region, 27 28 which explains the location of Moiré patterns observed on HRTEM image (Figure 2f). Taken 29 together, we concluded that Cu NRs possess a pentagonally twinned structure bounded by five {100}-facets on the sides and capped with five {111} facets at both ends. 30

Figure 3a-i present TEM images of a collection of Cu NRs synthesized using 9 nm Au seeds. The AR can be continuously adjusted from 2.8 to 13.1 by lowering the concentration of Au seeds while using the same concentration of CuCl<sub>2</sub> (Figure 31 and Table S1). Ultralong Cu NRs with a high AR of 35 were accessible upon further reduction in [Au seeds]/[CuCl<sub>2</sub>] ratio (Figure S3). The AR tunability arose primarily from variations in NR length as the diameter remained essentially fixed at about 12.5 nm (Figure 3f-j). HRTEM and electron diffraction analyses revealed that all NRs have a penta-twinned structure (Figure S4-S5). XRD patterns of different samples showed excellent agreement with predicted peak positions of the fcc Au<sub>0.03</sub>Cu<sub>0.97</sub> structure, suggesting low Au contents in NRs regardless of AR (Figure 3m). To enhance colloidal stability, native OLAM ligands on NRs were exchanged for thiol-terminated polystyrene (PS-SH). PS-grafted NRs readily formed close-packed monolayer assemblies over extended areas (Figure S6-S8), which not only demonstrates ensemble-level size uniformity, but also facilitates statistical analysis of NR dimensions (Figure S9-S10). A photograph of different NRs dispersed in toluene is shown in Figure 3k. The color of short NRs (AR=2.8) appeared to be black, indicative of broadband extinction in the visible region. In contrast, NRs with ARs exceeding 5 displayed a reddish color, suggesting that their LSPR has been shifted well into the NIR region.

Figure 4a shows extinction spectra of Cu NRs dispersed in tetrachloroethylene (TCE). The LSPR red-shifted from 762 to 2201 nm as the AR increased gradually from 2.8 to 13.1. A sharp LSPR was observed for every sample (e.g., fwhm = 0.468 eV for AR=4.9; fwhm = 0.397 eV for AR=9.0). To our knowledge, the spectral tunability shown in Figure 4a represents the broadest SPR tuning range to date for colloidal Cu-based NCs. We performed finite-difference time-domain (FDTD) simulations to gain a deeper understanding of the factors that dictate LSPR characteristics especially the impact of surface oxidation (Figure S12-S13). Appreciable discrepancies were found between experimental and simulated extinction spectra when metallic copper was assumed in simulations (Figure S12 and Table S2). To reconcile the disparity between theory and experiment, a Cu@Cu<sub>2</sub>O core/shell model was adopted and the thickness of the conformal Cu<sub>2</sub>O layer was varied until an excellent agreement was attained (Figure 4b and Figure S14). The optimal oxide layer thickness retrieved was less than 1.2 nm for different NRs, which is in line with HRTEM and XRD data (Table S2). Furthermore, experimental LSPR wavelength was found to vary linearly with AR via the relationship  $\lambda$  (nm) = 144.3 × AR + 381.3 (Figure 4c and Figure S15), which provides a useful guideline for synthesis of Cu NRs targeting specific LSPR

wavelengths. To our knowledge, analogous experimentally derived scaling relationships over a wide range of ARs are largely unavailable for metal NRs with the exception of gold NRs, for which  $\lambda (nm) = 96 \times AR + 418.^{32}$  Figure 4d-f show near-field enhancement (NFE) maps of three Cu@Cu<sub>2</sub>O NRs excited at their LSPR peak wavelengths. NFE factors in the range of 25-47 were retrieved even when a thin Cu<sub>2</sub>O layer was considered. These values are on par with other NIR plasmonic nanomaterials such as gold NRs and Sn-doped In<sub>2</sub>O<sub>3</sub> NCs,<sup>33</sup> demonstrating the potential of Cu NRs for surface-enhanced spectroscopy and sensing applications.

8

9

10

11

12

13

14

15

16

17

18 19

20

21

22

23

24

25

26

27

28

29

30

31

To understand the growth mechanism of Cu NRs, reaction intermediates were examined using multiple analytical techniques. Within 8 min after seed injection, NCs remained spherical while the mean diameter increased from 8.6 to 11.3 nm (Figure S16a-e and Figure S17). Concurrently, a gradual redshift in SPR from 517 to 550 nm was observed, indicating that Cu was diffusing into Au forming Au-Cu alloy (Figure S16f). This is consistent with previous reports of diffusionmediated synthesis of Au-Cu alloy NCs at elevated temperatures. 34-36 In fact, it is well established that bulk Cu and Au form solid solutions with continuously tunable alloy compositions. <sup>35, 37, 38</sup> The onset of anisotropic growth began at approximately 8-10 min when the solution color changed from red to black, yielding a mixture of spherical and elongated particles (Figure 5b). STEM-EDS elemental mapping and HRTEM imaging revealed that these intermediates are Au-Cu alloys with spatially varying composition and surface enrichment of Au. (Figure 5f-g and Figure S18). Furthermore, EDS line profile indicated that the small protrusion grown out of the seed was largely comprised of gold (Figure 5f). Surface segregation of gold in Au-Cu alloys can be rationalized based on thermodynamic arguments. First, it is generally more favorable to have larger atoms (gold in this case) occupy surface sites because such arrangement will result in less surface atoms thereby lowering the overall energy due to bond breaking.<sup>37, 38</sup> Second, element with the smallest surface energy (also gold in this case) tends to populate the surface (cf.  $\gamma_{Cu(111)} = 1.83 \text{ J/m}^2$ ,  $\gamma_{Au(111)} = 1.50$ J/m<sup>2</sup>).<sup>39, 40</sup> XRD pattern of the 10-min reaction aliquot was best matched to the AuCu<sub>3</sub> phase (Figure 51). The absence of superlattice peaks at  $2\theta=33.8^{\circ}$  indicates that atomically disordered fcc alloy was formed, 41 likely due to the rapid interdiffusion of Au and Cu and relatively low reaction temperature (i.e., 180 °C). At 20 min, symmetry breaking had taken place on a large proportion of Au seeds (Figure 5c,h), generating elongated NCs with an undulating surface morphology (Figure 5h). A broad extinction band centered at 1238 nm was observed, which signifies the presence of high-aspect-ratio rod-like particles in the reaction mixture (Figure 5k). Moreover, XRD peaks had

1 shifted to higher angles compared to 10-min intermediates, suggesting a further increase in Cu content (Figure 51).<sup>35</sup> Subsequent Cu deposition lengthened the NCs, causing LSPR to red-shift to 2 3 1729 nm after 30 min of reaction (Figure 5d, 5i and 5k). The presence of grooves with a negative surface curvature can render the structure energetically unstable. Consequently, further deposition 4 of Cu atoms and surface diffusion are expected to smooth out these rough features, thereby 5 lowering the total surface energy. Indeed, straight NRs with a minimal surface roughness and a 6 7 minute amount of gold were obtained after 1h (Figure 5e,j). A pronounced LSPR band centered at 1483 nm (fwhm= 0.404 eV) was observed, supporting the high crystallinity of NRs and reduced 8 scattering from surface imperfections (Figure 51). 9

10

11

12

13

14

15

16

17

18

19

20

21

22

23

24

25

26

27

28

29

30

We further quantified the composition of reaction intermediates using EDS and XRD. The Cu at. % determined from SEM-EDS was 74%, 83%, 93%, and 98 % for samples obtained after 10, 20, 30 and 60 minutes of reaction, respectively, in good agreement with atomic ratios determined from STEM-EDS (Figure 5m). Besides, XRD provides an independent measure of time-dependent alloy compositions. Application of Vegard's law to XRD-derived lattice constant returns atomic percentages of constituent elements.<sup>35</sup> The Cu at. % retrieved from XRD analysis were 69%, 80%, 90% and 96% for NCs obtained at 10, 20, 30, and 60 min, respectively (Figure 5m, Table S3, Figure S19). Both XRD and EDS data indicate that NCs became progressively enriched with Cu accompanying growth from spherical seeds to NRs. Although reaction intermediates exhibited a wavy surface morphology, which could have resulted from fusion of NCs, additional experimental evidence indicated that an aggregative growth or orientated attachment mechanism is highly unlikely. First, a monotonic increase in AR was achieved when the [Au seeds]/[CuCl<sub>2</sub>] ratio was lowered (Figure 31). On the contrary, an opposite trend in or a lack of AR tunability would have resulted if NRs were formed through coalescence of NCs. Second, the Au content of NRs was consistently below 6.5% irrespective of AR (Figure 5m and Figure S20), which is in line with predictions of a basic geometrical model assuming that (1) each NR derives from one Au seed, and (2) dissolution of Au atoms into reaction solution is insignificant (Figure S20 and Table S4-S5).

The crude products contained ca. 5% of spherical NCs that are removed via size-selective precipitation (Figure S21-S22). Importantly, the Cu contents of spherical NCs were found to essentially mirror the compositional evolution of rod-shaped counterparts (Figure S22c-e and

Figure S23). Therefore, it appears that anisotropic growth commenced on a vast majority of seeds within a relatively short period of time, after which elongated NCs continued to develop into NRs while the rest remained as spheres. One reason for the co-generation of spheres and NRs is a distribution in the onset of anisotropic growth causing delayed symmetry breaking events for some seeds. However, we believe that this mechanism is unlikely given the uniformity in size, shape, and surface chemistry of Au seeds. A more plausible explanation is a distribution of single-crystalline versus penta-twinned seeds. As previously demonstrated for different metals, the presence of twin planes in seed NCs can be a decisive factor for promoting anisotropic growth. 42, <sup>43</sup> Although the penta-twinned structure was theoretically predicted and experimentally shown to be more stable than single-crystal for small Au NCs, 44 one cannot rule out the presence of a small amount of single-crystalline seeds, which may persist as spherical entities throughout the reaction. Likewise, twin planes may be generated in situ, which has been shown during deposition of Cu onto Au (100) single crystal and single-crystalline Au NCs. 24, 45 

To elucidate the important roles of atom diffusion, a thermally activated process, in controlling anisotropic growth, reactions were run at temperatures ranging from 80 °C to 240 °C. Only spherical NCs were produced at less than 160 °C (Figure S24). Further, a monotonic increase in NC size was realized at increasing temperatures:  $9.3 \pm 0.4$  nm (80 °C),  $10.0 \pm 0.5$  nm (120 °C) and  $11.2 \pm 0.5$  nm (140 °C), suggesting that Cu diffusion into Au seeds already occurred at 80 °C. The lowest temperature for activation of anisotropic growth was found to be 160 °C, with 180 °C being the optimal temperature judged by the uniformity and yield of NRs (Figure S25).

## **CONCLUSION**

In summary, we have developed a heterometallic seed-mediated synthesis method for monodisperse penta-twinned Cu NRs using preformed Au seeds. The AR can be continuously varied from 2.8 to 13.1 by reducing the molar ratio between Au seeds and Cu precursor, resulting in narrow LSPRs tunable from 762 to 2201 nm. Studies of reaction intermediates revealed that initial symmetry-breaking is facilitated by rapid nanoscale diffusion in Au-Cu alloys and coincides with the formation of elongated NCs with a gold-rich surface. NCs became progressively enriched in copper and eventually yielded well-defined NRs. The detailed reaction pathway uncovered may inform new strategies for shape-controlled synthesis of Cu NCs. Furthermore, the availability of Cu NRs with widely tunable ARs will open up a rich design space for derivative one-dimensional

1 mono- and multi-metallic nanostructures, and will enable new applications in surface-enhance	anced
--	-------

2 spectroscopy, bioimaging, electrocatalysis, etc.

## ASSOCIATED CONTENT

- 2 Supporting Information. Experimental section, structural characterization of Cu NRs, FDTD
- 3 simulation results and studies of reaction intermediates are included. This material is available free
- 4 of charge via the Internet at http://pubs.acs.org.

5

1

## **6 AUTHOR INFORMATION**

- 7 Corresponding Author
- \* Correspondence should be addressed to Prof. Xingchen Ye (xingye@indiana.edu)
- 9 Funding Sources
- 10 The authors acknowledge financial support from Indiana University through the FRSP-Seed
- program and National Science Foundation under award number CHE-1808027.
- 12 Notes
- 13 The authors declare no competing financial interest.

14

## 15 ACKNOWLEDGMENT

- We thank Prof. Amar Flood for use of UV-Vis-NIR spectrometer and Prof. Bogdan Dragnea for
- 17 access of FDTD simulation software. We thank Indiana University Nanoscale Characterization
- 18 Facility and Electron Microscopy Center for access of instrumentation.

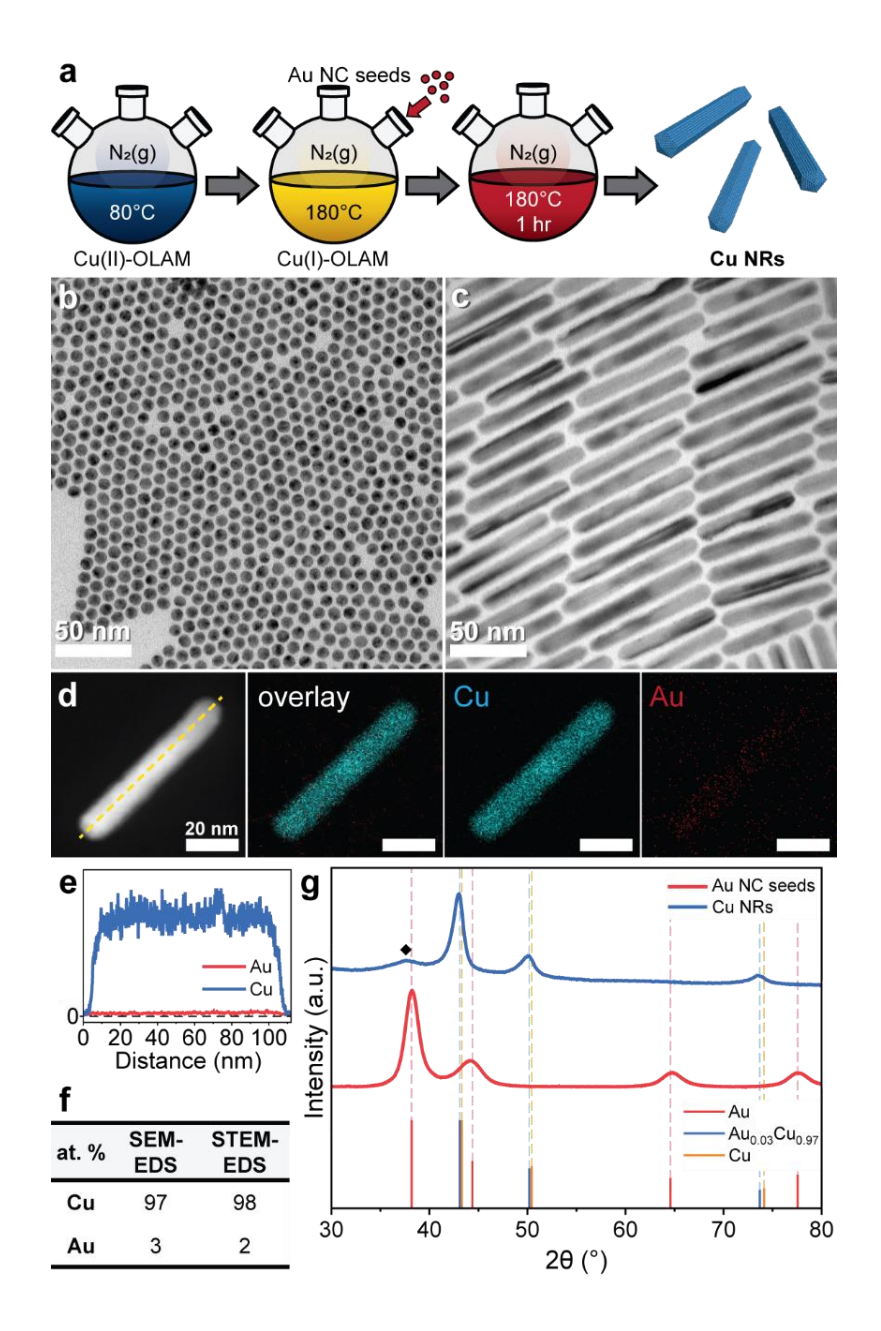
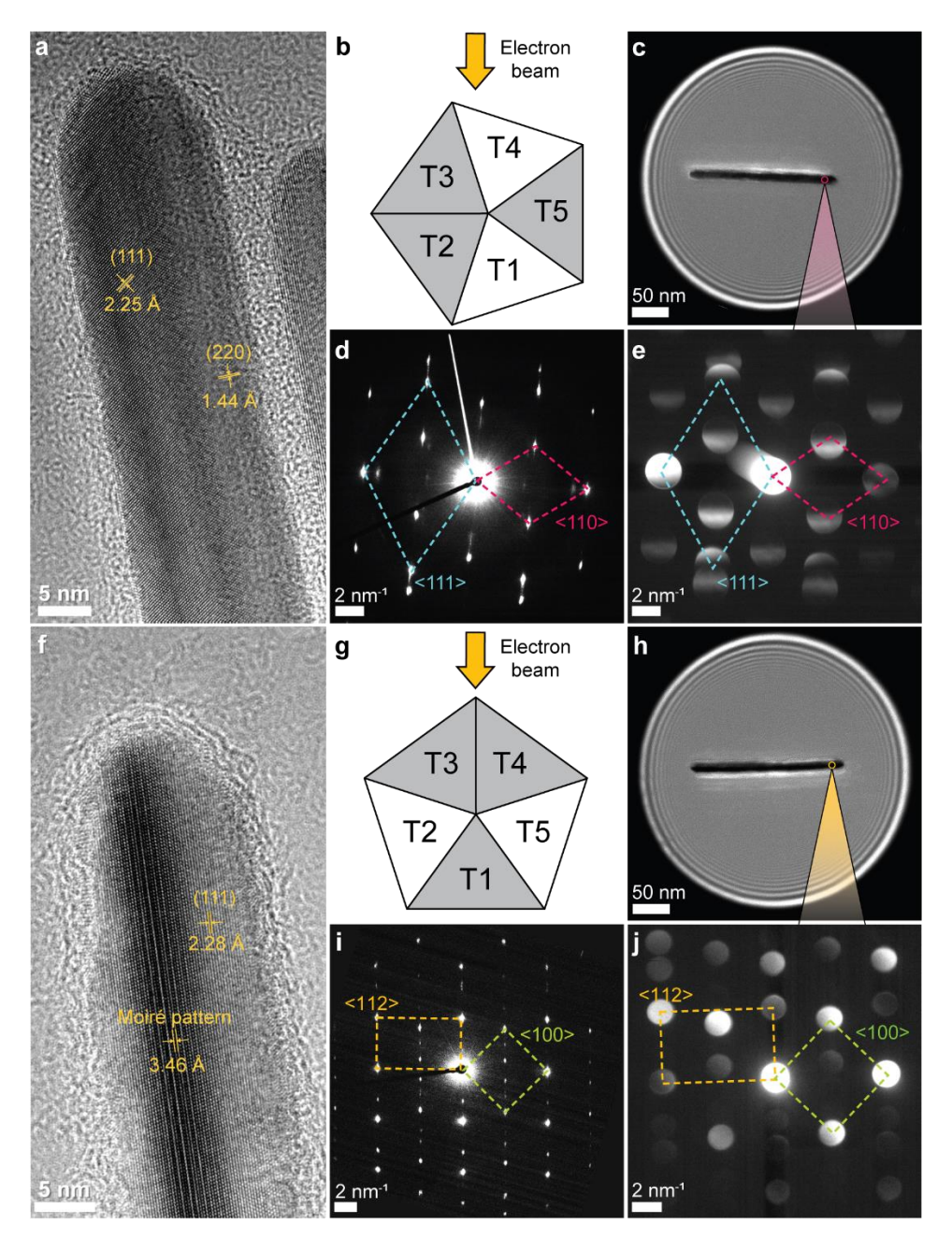
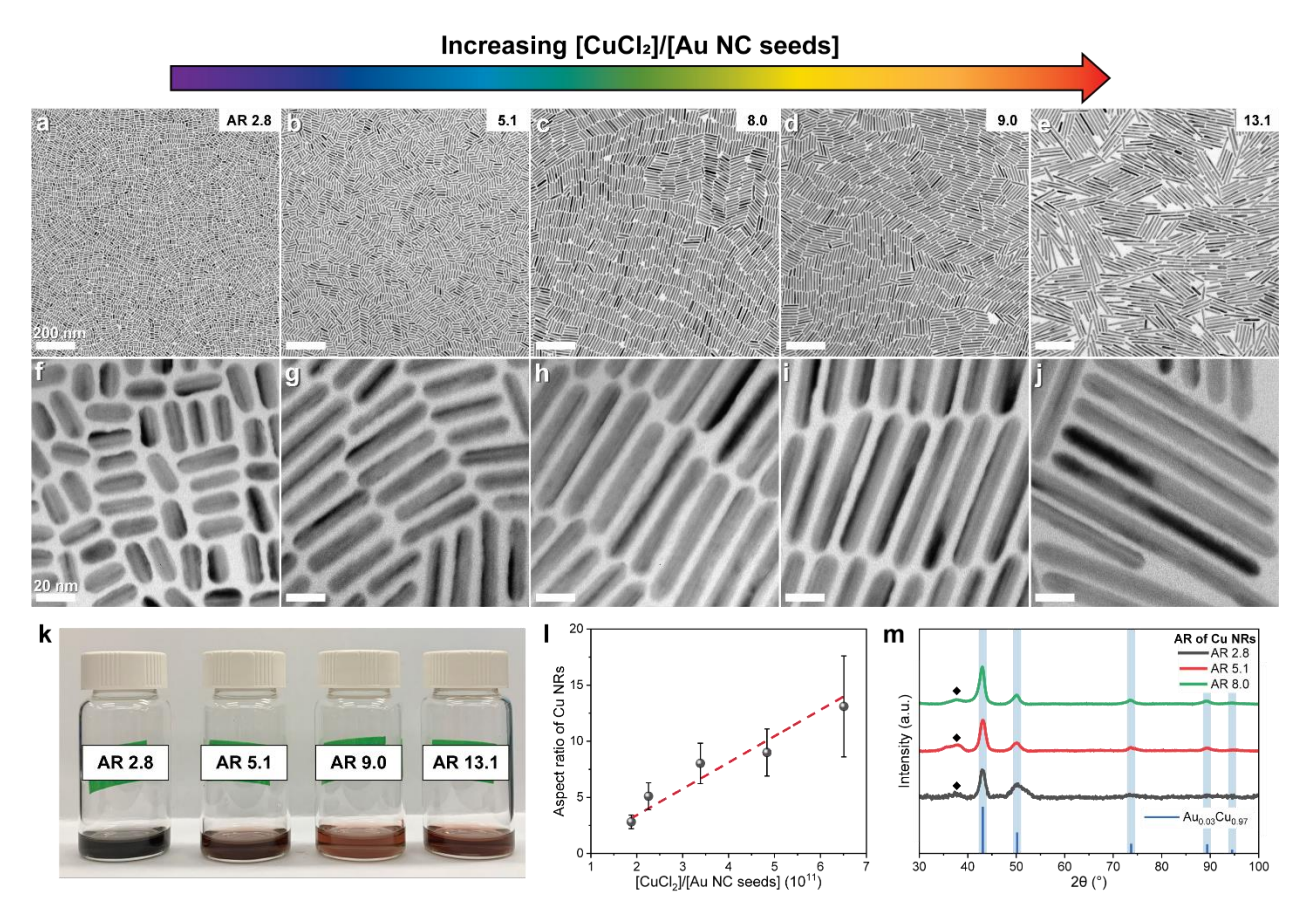


Figure 1. (a) Scheme of seeded growth of Cu NRs using preformed Au NCs as seeds. (b,c) TEM image of 9 ± 0.4 nm Au NC seeds (b) and resulting Cu NRs (c). (d) HAADF-STEM image and STEM-EDS elemental maps of a single Cu NR. (e) STEM-EDS line profiles of Cu and Au contents along the yellow dashed line indicated in (d). (f) Elemental analysis results of Cu NRs. (g) XRD patterns of 5.5 nm Au NC seeds and Cu NRs. The vertical bars at the bottom represent the standard diffraction patterns of Au (JCPDS card no. 00-004-0784), Au<sub>0.03</sub>Cu<sub>0.97</sub> (JCPDS card no. 01-077-6964), and Cu (JCPDS card no. 00-004-0836). The additional peak centered at 37.5° is attributed to Cu<sub>2</sub>O due to surface oxidation of Cu NRs.



**Figure 2.** Structural analysis of penta-twinned Cu NRs. (a) HRTEM image of a Cu NR with one of its five side facets parallel to the electron beam, as illustrated by the cross-sectional scheme in (b). (c-e) CNED (d) and NBED (e) patterns acquired from the NR shown in (c). (f) HRTEM image of a Cu NR with one of its five side facets orthogonal to the electron beam, as illustrated by the cross-sectional scheme in (g). (h-j) CNED (i) and NBED (j) patterns acquired from the NR shown in (h). CNED patterns were recorded from the circular area defined by the condenser aperture shown in (c) and (h) covering the entire NR. NBED patterns were recorded from the circular spot (2-nm full-width at half-maximum) near the end of NR as indicated on (c) and (h).



**Figure 3.** Synthetic tuning of Cu NR aspect ratio. (a-j) Low-magnification (a-e) and high-magnification (f-j) TEM images of Cu NRs with the average AR of 2.8 (a,f), 5.1 (b,g), 8.0 (c,h), 9.0 (d,i), and 13.1 (e,j). (k) Photograph of Cu NRs with various aspect ratios dispersed in toluene. (l) Plot of Cu NR aspect ratio versus the [CuCl<sub>2</sub>]/ [Au NC seeds] ratio. (m) Representative XRD patterns of Cu NRs with the average AR of 2.8 (black), 5.1 (red), and 8.0 (green). The vertical bars at the bottom represent the standard diffraction pattern of Au<sub>0.03</sub>Cu<sub>0.97</sub> (JCPDS card no. 01-077-6964). The additional peak centered at 37.5° is attributed to Cu<sub>2</sub>O due to surface oxidation of Cu NRs. Scale bars: (a-e) 200 nm, (f-j) 20 nm.

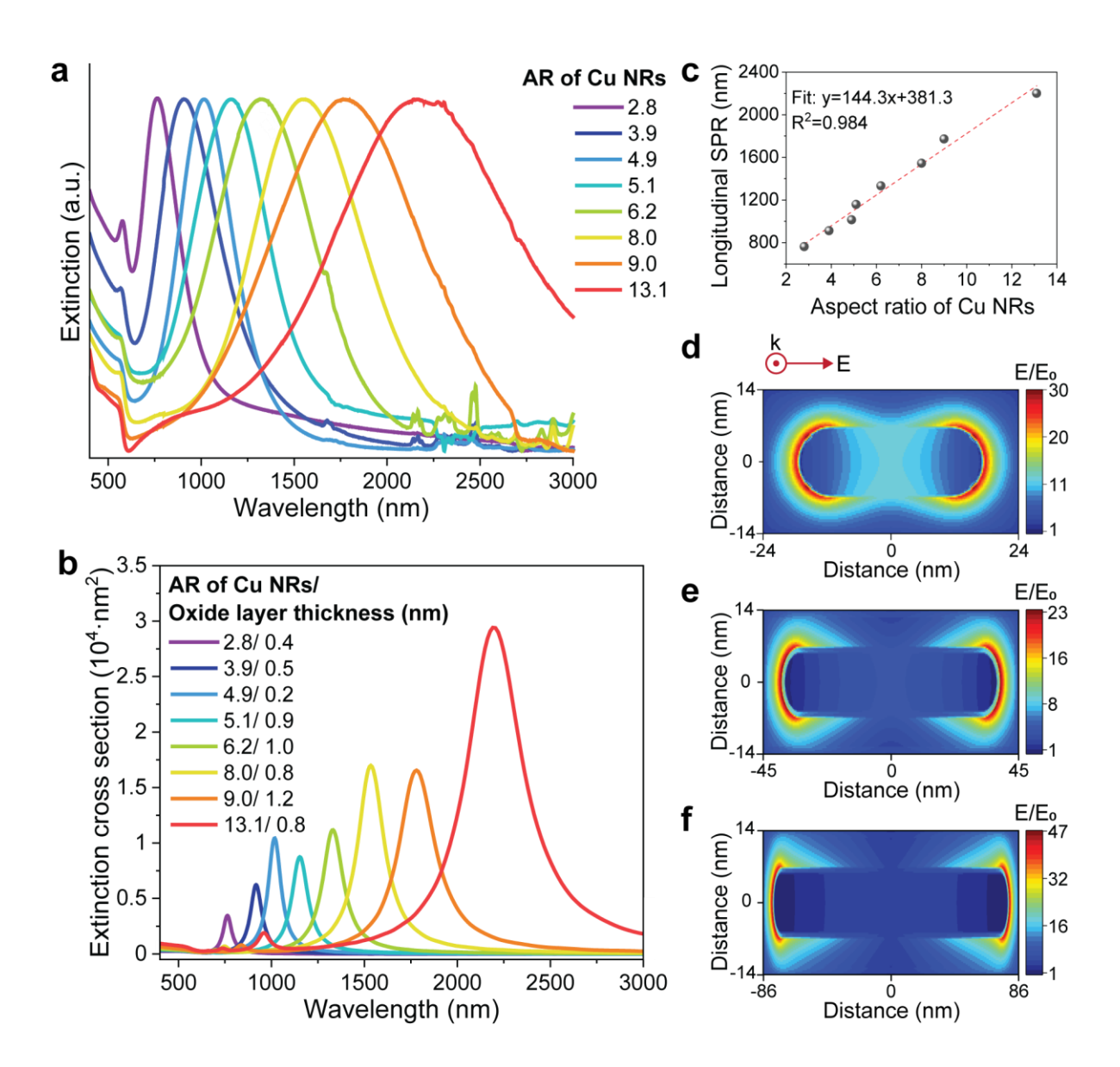


**Figure 4.** Plasmonic properties of Cu NRs with various aspect ratios. (a) UV-Vis-NIR extinction spectra of Cu NRs with aspect ratios ranging from 2.8 to 13.1 and resulting LSPR tunable from 762 to 2201 nm. (b) FDTD simulated extinction spectra of Cu NRs covered with a thin surface oxide layer. The direction of polarization was set to be parallel to the long-axis of NR. The NR aspect ratio and surface oxide thickness are provided in the legend. (c) Plot of experimental LSPR peak wavelength versus NR aspect ratio. The red dashed line represents the linear fit to the data. (d-f) FDTD simulated NFE maps of Cu NRs covered with a thin surface oxide layer with the AR of 2.8 (d), 6.2 (e) and 13.1 (f). NFE maps were calculated for the extinction peak wavelength of 763 nm (d), 1330 nm (e) and 2198 nm (f).

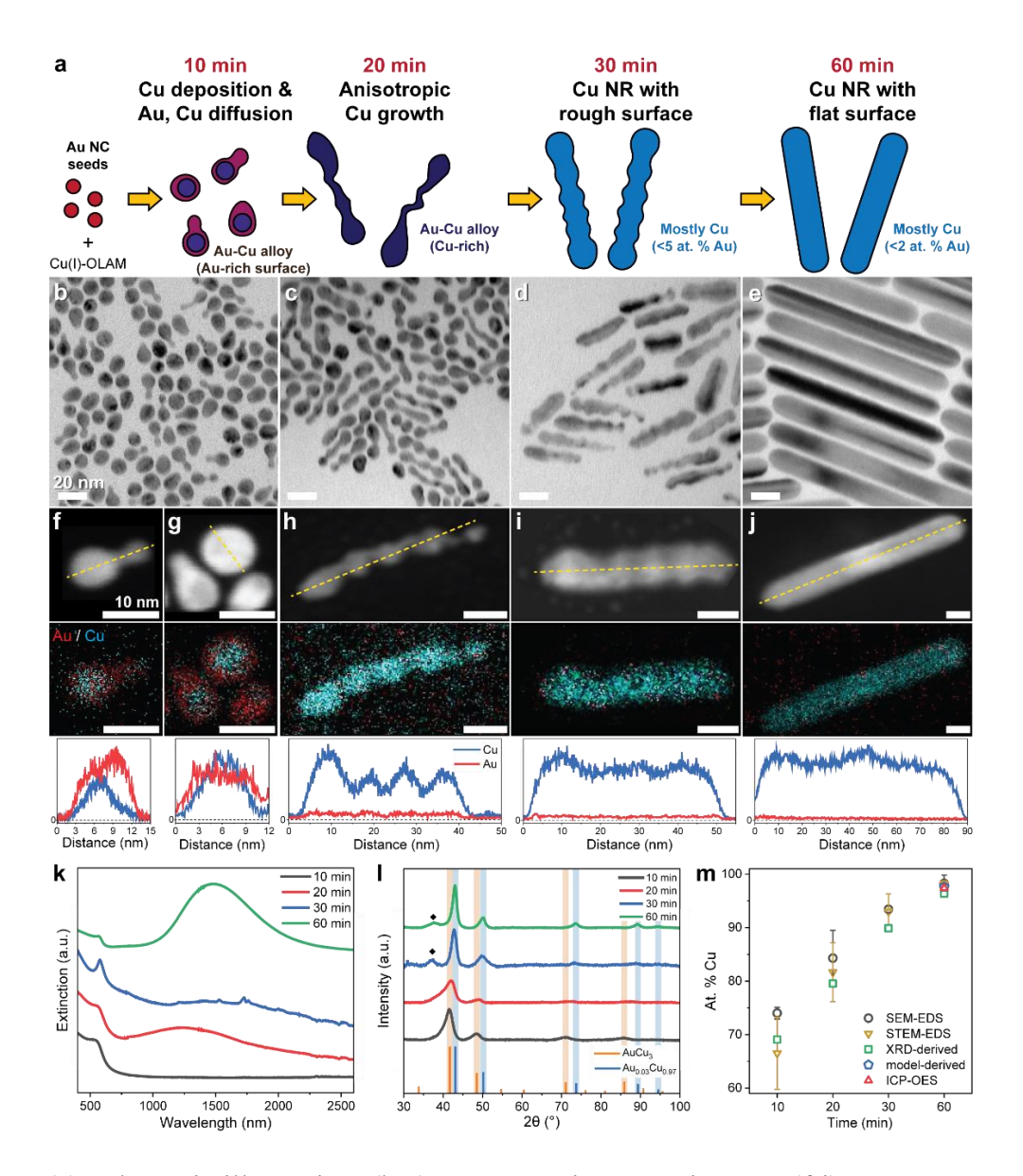


**Figure 5.** (a) Schematic illustration, (b-e) representative TEM images, (f-j) STEM-EDS analysis results and (k) UV-Vis-NIR extinction spectra of reaction intermediates of Cu NRs synthesized using 9 nm Au NCs as seeds. Scale bars: 20 nm (b-e) and 10 nm (f-j). (l) XRD patterns of reaction intermediates produced during synthesis of Cu NRs. The vertical bars at the bottom represent the standard diffraction pattern of bulk AuCu<sub>3</sub> (JCPDS card no. 00-035-1357) and Au<sub>0.03</sub>Cu<sub>0.97</sub> (JCPDS card no. 01-077-6964). (m) Plots of Cu contents of different reaction intermediates determined from SEM-EDS analysis (black circles), STEM-EDS analysis (yellow triangles), and XRD peak analysis and Vegard's law (green squares). The percent copper of Cu NRs calculated based on a geometrical model (blue pentagon) and Cu contents measured by ICP-OES (red triangles) are also shown for comparison.

## Reference

- 1. Huo, D.; Kim, M. J.; Lyu, Z.; Shi, Y.; Wiley, B. J.; Xia, Y. One-Dimensional Metal Nanostructures: From Colloidal Syntheses to Applications. *Chem. Rev.* **2019**, *119*, 8972-9073.
- 2. Nikoobakht, B.; El-Sayed, M. A. Preparation and Growth Mechanism of Gold Nanorods (NRs) Using Seed-Mediated Growth Method. *Chem. Mater.* **2003**, *15*, 1957-1962.
- 3. Ye, X.; Zheng, C.; Chen, J.; Gao, Y.; Murray, C. B. Using Binary Surfactant Mixtures to Simultaneously Improve the Dimensional Tunability and Monodispersity in the Seeded Growth of Gold Nanorods. *Nano Lett.* **2013**, *13*, 765-771.
- 4. Jana, N. R.; Gearheart, L.; Murphy, C. J. Wet Chemical Synthesis of Silver Nanorods and Nanowires of Controllable Aspect Ratio. *Chem. Comm.* **2001**, 617-618.
- 5. Wiley, B. J.; Chen, Y.; McLellan, J. M.; Xiong, Y.; Li, Z.-Y.; Ginger, D.; Xia, Y. Synthesis and Optical Properties of Silver Nanobars and Nanorice. *Nano Lett.* **2007**, *7*, 1032-1036.
- 6. Zhang, J.; Langille, M. R.; Mirkin, C. A. Synthesis of Silver Nanorods by Low Energy Excitation of Spherical Plasmonic Seeds. *Nano Lett.* **2011**, *11*, 2495-2498.
- 7. Lal, S.; Grady, N. K.; Kundu, J.; Levin, C. S.; Lassiter, J. B.; Halas, N. J. Tailoring Plasmonic Substrates for Surface Enhanced Spectroscopies. *Chem. Soc. Rev.* **2008**, *37*, 898-911.
- 8. Alvarez-Puebla, R. A.; Agarwal, A.; Manna, P.; Khanal, B. P.; Aldeanueva-Potel, P.; Carbó-Argibay, E.; Pazos-Pérez, N.; Vigderman, L.; Zubarev, E. R.; Kotov, N. A.; Liz-Marzán, L. M. Gold Nanorods 3D-Supercrystals as Surface Enhanced Raman Scattering Spectroscopy Substrates for the Rapid Detection of Scrambled Prions. *Proc. Natl. Acad. Sci.* **2011**, *108*, 8157-8161.
- 9. Wu, B.; Liu, D.; Mubeen, S.; Chuong, T. T.; Moskovits, M.; Stucky, G. D. Anisotropic Growth of TiO<sub>2</sub> onto Gold Nanorods for Plasmon-Enhanced Hydrogen Production from Water Reduction. *J. Am. Chem. Soc.* **2016**, *138*, 1114-1117.
- 10. Dreaden, E. C.; Alkilany, A. M.; Huang, X.; Murphy, C. J.; El-Sayed, M. A. The Golden Age: Gold Nanoparticles for Biomedicine. *Chem. Soc. Rev.* **2012**, *41*, 2740-2779.
- 11. Rathmell, A. R.; Bergin, S. M.; Hua, Y.-L.; Li, Z.-Y.; Wiley, B. J. The Growth Mechanism of Copper Nanowires and Their Properties in Flexible, Transparent Conducting Films. *Adv. Mater.* **2010**, *22*, 3558-3563.
- 12. Cui, F.; Yu, Y.; Dou, L.; Sun, J.; Yang, Q.; Schildknecht, C.; Schierle-Arndt, K.; Yang, P. Synthesis of Ultrathin Copper Nanowires Using Tris(trimethylsilyl)silane for High-Performance and Low-Haze Transparent Conductors. *Nano Lett.* **2015**, *15*, 7610-7615.
- 13. Jouny, M.; Luc, W.; Jiao, F. High-Rate Electroreduction of Carbon Monoxide to Multi-Carbon Products. *Nature Catal.* **2018**, *1*, 748-755.
- 14. Behrens, M.; Studt, F.; Kasatkin, I.; Kühl, S.; Hävecker, M.; Abild-Pedersen, F.; Zander, S.; Girgsdies, F.; Kurr, P.; Kniep, B.-L.; Tovar, M.; Fischer, R. W.; Nørskov, J. K.; Schlögl, R. The Active Site of Methanol Synthesis over Cu/ZnO/Al<sub>2</sub>O<sub>3</sub> Industrial Catalysts. *Science* **2012**, *336*, 893-897.
- 15. Son, S. U.; Park, I. K.; Park, J.; Hyeon, T. Synthesis of Cu<sub>2</sub>O Coated Cu Nanoparticles and Their Successful Applications to Ullmann-Type Amination Coupling Reactions of Aryl Chlorides. *Chem. Comm.* **2004**, 778-779.

- 16. Chan, G. H.; Zhao, J.; Hicks, E. M.; Schatz, G. C.; Van Duyne, R. P. Plasmonic Properties of Copper Nanoparticles Fabricated by Nanosphere Lithography. *Nano Lett.* **2007**, *7*, 1947-1952.
- 17. Hung, L. I.; Tsung, C. K.; Huang, W.; Yang, P. Room-Temperature Formation of Hollow Cu<sub>2</sub>O Nanoparticles. *Adv. Mater.* **2010**, *22*, 1910-1914.
- 18. Jin, M.; He, G.; Zhang, H.; Zeng, J.; Xie, Z.; Xia, Y. Shape-Controlled Synthesis of Copper Nanocrystals in an Aqueous Solution with Glucose as a Reducing Agent and Hexadecylamine as a Capping Agent. *Angew. Chem. Int. Ed.* **2011**, *50*, 10560-10564.
- 19. Strach, M.; Mantella, V.; Pankhurst, J. R.; Iyengar, P.; Loiudice, A.; Das, S.; Corminboeuf, C.; Beek, W. V.; Buonsanti, R. Insights into Reaction Intermediates to Predict Synthetic Pathways for Shape-Controlled Metal Nanocrystals. *J. Am. Chem. Soc.* **2019**, *141*, 16312-16322.
- 20. Kim, M. J.; Alvarez, S.; Chen, Z.; Fichthorn, K. A.; Wiley, B. J. Single-Crystal Electrochemistry Reveals Why Metal Nanowires Grow. *J. Am. Chem. Soc.* **2018**, *140*, 14740-14746.
- 21. Luo, M.; Ruditskiy, A.; Peng, H.-C.; Tao, J.; Figueroa-Cosme, L.; He, Z.; Xia, Y. Penta-Twinned Copper Nanorods: Facile Synthesis Via Seed-Mediated Growth and Their Tunable Plasmonic Properties. *Adv. Funct. Mater.* **2016**, *26*, 1209-1216.
- 22. Tanori, J.; Pileni, M. P. Control of the Shape of Copper Metallic Particles by Using a Colloidal System as Template. *Langmuir* **1997**, *13*, 639-646.
- 23. Mott, D.; Galkowski, J.; Wang, L.; Luo, J.; Zhong, C.-J. Synthesis of Size-Controlled and Shaped Copper Nanoparticles. *Langmuir* **2007**, *23*, 5740-5745.
- 24. Wang, Z.; Chen, Z.; Zhang, H.; Zhang, Z.; Wu, H.; Jin, M.; Wu, C.; Yang, D.; Yin, Y. Lattice-Mismatch-Induced Twinning for Seeded Growth of Anisotropic Nanostructures. *ACS Nano* **2015**, *9*, 3307-3313.
- 25. Chen, J.; Feng, J.; Yang, F.; Aleisa, R.; Zhang, Q.; Yin, Y. Space-Confined Seeded Growth of Cu Nanorods with Strong Surface Plasmon Resonance for Photothermal Actuation. *Angew. Chem. Int. Ed.* **2019**, *58*, 9275-9281.
- 26. Henkel, A.; Jakab, A.; Brunklaus, G.; Sönnichsen, C. Tuning Plasmonic Properties by Alloying Copper into Gold Nanorods. *J. Phys. Chem. C* **2009**, *113*, 2200-2204.
- 27. Chen, S.; Jenkins, S. V.; Tao, J.; Zhu, Y.; Chen, J. Anisotropic Seeded Growth of Cu–M (M = Au, Pt, or Pd) Bimetallic Nanorods with Tunable Optical and Catalytic Properties. *J. Phys. Chem. C* **2013**, *117*, 8924-8932.
- 28. Wang, X.; Chen, S.; Reggiano, G.; Thota, S.; Wang, Y.; Kerns, P.; Suib, S. L.; Zhao, J. Au-Cu-M (M = Pt, Pd, Ag) Nanorods with Enhanced Catalytic Efficiency by Galvanic Replacement Reaction. *Chem. Comm.* **2019**, *55*, 1249-1252.
- 29. Shah, A. B.; Sivapalan, S. T.; DeVetter, B. M.; Yang, T. K.; Wen, J.; Bhargava, R.; Murphy, C. J.; Zuo, J.-M. High-Index Facets in Gold Nanocrystals Elucidated by Coherent Electron Diffraction. *Nano Lett.* **2013**, *13*, 1840-1846.
- 30. Lisiecki, I.; Filankembo, A.; Sack-Kongehl, H.; Weiss, K.; Pileni, M. P.; Urban, J. Structural Investigations of Copper Nanorods by High-Resolution Tem. *Phys. Rev. B* **2000**, *61*, 4968-4974.
- 31. Johnson, C. J.; Dujardin, E.; Davis, S. A.; Murphy, C. J.; Mann, S. Growth and Form of Gold Nanorods Prepared by Seed-Mediated, Surfactant-Directed Synthesis. *J. Mater. Chem.* **2002**, *12*, 1765-1770.

- 32. Brioude, A.; Jiang, X. C.; Pileni, M. P. Optical Properties of Gold Nanorods: DDA Simulations Supported by Experiments. *J. Phys. Chem. B* **2005**, *109*, 13138-13142.
- 33. Khatua, S.; Paulo, P. M. R.; Yuan, H.; Gupta, A.; Zijlstra, P.; Orrit, M. Resonant Plasmonic Enhancement of Single-Molecule Fluorescence by Individual Gold Nanorods. *ACS Nano* **2014**, *8*, 4440-4449.
- 34. Chen, W.; Yu, R.; Li, L.; Wang, A.; Peng, Q.; Li, Y. A Seed-Based Diffusion Route to Monodisperse Intermetallic CuAu Nanocrystals. *Angew. Chem. Int. Ed.* **2010**, *49*, 2917-2921.
- 35. Motl, N. E.; Ewusi-Annan, E.; Sines, I. T.; Jensen, L.; Schaak, R. E. Au-Cu Alloy Nanoparticles with Tunable Compositions and Plasmonic Properties: Experimental Determination of Composition and Correlation with Theory. *J. Phys. Chem. C* **2010**, *114*, 19263-19269.
- 36. Zhan, W.; Wang, J.; Wang, H.; Zhang, J.; Liu, X.; Zhang, P.; Chi, M.; Guo, Y.; Guo, Y.; Lu, G.; Sun, S.; Dai, S.; Zhu, H. Crystal Structural Effect of AuCu Alloy Nanoparticles on Catalytic CO Oxidation. *J. Am. Chem. Soc.* **2017**, *139*, 8846-8854.
- 37. Guisbiers, G.; Mejia-Rosales, S.; Khanal, S.; Ruiz-Zepeda, F.; Whetten, R. L.; Jose-Yacaman, M. Gold-Copper Nano-Alloy, "Tumbaga", in the Era of Nano: Phase Diagram and Segregation. *Nano Lett.* **2014**, *14*, 6718-6726.
- 38. Thota, S.; Wang, Y.; Zhao, J. Colloidal Au–Cu Alloy Nanoparticles: Synthesis, Optical Properties and Applications. *Mater. Chem. Front.* **2018**, *2*, 1074-1089.
- 39. Skriver, H. L.; Rosengaard, N. M. Surface Energy and Work Function of Elemental Metals. *Phys. Rev. B* **1992**, *46*, 7157-7168.
- 40. Osowiecki, W. T.; Ye, X.; Satish, P.; Bustillo, K. C.; Clark, E. L.; Alivisatos, A. P. Tailoring Morphology of Cu–Ag Nanocrescents and Core–Shell Nanocrystals Guided by a Thermodynamic Model. *J. Am. Chem. Soc.* **2018**, *140*, 8569-8577.
- 41. Ashberry, H. M.; Gamler, J. T. L.; Unocic, R. R.; Skrabalak, S. E. Disorder-to-Order Transition Mediated by Size Refocusing: A Route toward Monodisperse Intermetallic Nanoparticles. *Nano Lett.* **2019**, *19*, 6418-6423.
- 42. O'Brien, M. N.; Jones, M. R.; Brown, K. A.; Mirkin, C. A. Universal Noble Metal Nanoparticle Seeds Realized through Iterative Reductive Growth and Oxidative Dissolution Reactions. *J. Am. Chem. Soc.* **2014**, *136*, 7603-7606.
- 43. Sánchez-Iglesias, A.; Winckelmans, N.; Altantzis, T.; Bals, S.; Grzelczak, M.; Liz-Marzán, L. M. High-Yield Seeded Growth of Monodisperse Pentatwinned Gold Nanoparticles through Thermally Induced Seed Twinning. *J. Am. Chem. Soc.* **2017**, *139*, 107-110.
- 44. Marks, L. D. Surface Structure and Energetics of Multiply Twinned Particles. *Philos. Mag. A* **1984**, *49*, 81-93.
- 45. Randler, R.; Dietterle, M.; Kolb, D. M. The Initial Stages of Cu Deposition on Au(100) as Studied by In Situ STM: The Epitaxial Growth of bcc Cu. *Z. Phys. Chem.* **1999**, *208*, 43-56.

## **Table of Contents Graphic**

